Surface Sulfurization and Self-Reconstruction Strategy for Decorating Carbon Nanofibers to Fabricate Sheet-Like NiCo$_2$S$_4$ Grown on Ni$_3$S$_2$ Electrode for High-Energy Density Asymmetric Supercapacitor

T. Arun,[a, b] K. Aravinth,*[a] P. Balaji Bhargav,[a] and Mani Govindasamy*[b, c]

In this study, transition metal sulfide-based binder-free hybrid electrodes were grown in-situ on Ni foam using hydrothermal method. However, it still remains a challenge for designing a heterostructure with sufficient electroactive sites to improve electrochemical performance. Herein, effects of CNF@NSNCS on Ni foam binder-free composites were investigated for developing high-performance, low-cost supercapacitors. By avoiding the use of additive binding polymers, the purity of the electrodes was enhanced, resulting in excellent electrochemical behavior. The prepared binder-free CNF@NSNCS composite electrode exhibited an ultrahigh specific capacitance of 2739 F/ g at a current density of 1 A/g, with superior capacitance retention charge-discharge cycle stability of 100% over continuous 14,000 cycles at 10 A/g. Furthermore, an asymmetric supercapacitor (ASC) was assembled using CNF@NSNCS binder-free composites as the positive electrode and Activated carbon (AC) as the negative electrode. The assembled devices demonstrated superior electrochemical performance, delivering a high energy density of 77.5 Wh/kg at a power density of 748.4 W/kg. This work may contribute to advancing the development of low-cost, high-performance energy storage applications for the next generation of portable electronic devices.

1. Introduction

Due to the increasing demand, scientific investigations are being focused in the search for a new generation of portable electronic devices, accompanied by the development of environmental friendly, fast charging, and high energy efficient materials.[1–3] Researchers have focused on supercapacitors (SCs) as an alternate solution for individual and hybrid applications alongside other storage devices. SCs possess several advantages, including superior power density, quick charge/discharge rates, and extended cycle lifespan, which have drawn considerable interest as battery substitutes.[4] These qualities make them excellent option for consumer electronics, energy backup systems, and hybrid electric cars. Significant progress has been achieved in creating high-performance SCs thus far. Supercapacitors are classified into two categories depending on charge storage mechanisms: electric double-layer capacitors and pseudocapacitors.[5,6] Pseudocapacitors exhibit better elec-trochemical performance compared to electric double-layer capacitors (EDLC) because EDLCs have very low energy density and poor electrochemical behavior compared to pseudocapacitors.[7–9] Many materials such as conducting polymers, metal oxides and/or hydroxides, carbon-based materials, metal-organic frameworks, and novel nanostructured transition metal dichalcogenides have been studied and are being explored as potential SC electrodes,.[10,11] Transition metal sulfides (TMS) have recently gained wide usage in electro-chemical storage applications due to their abundant electro-chemical activity, good electrical conductivity, and quick charge intercalation and de-intercalation across interfaces.[12,13] Mixed metal sulfide materials exhibit superior redox reactions and electrical conductivity compared to monometallic sulfides. Consequently, various metal sulfides and mixed metal sulfides, such as NiS$_2$, Ni$_3$S$_4$, Ni$_3$S$_2$, Ni$_7$S$_6$, Cu$_2$NiSnS$_4$, CuCo$_2$S$_4$, Cu$_2$ZnSnS$_4$, MnCo$_2$S$_4$, CoNi$_2$S$_4$, NiCo$_2$S$_4$, and ZnCo$_2$S$_4$, have proven to be reliable candidates for energy storage applications. In addition, Metal sulfides suffer from drawbacks such as significant volume changes during cycling, which can lead to structural collapse and pulverization, ultimately degrading electrochemical performance. To mitigate these issues and enhance the energy storage capabilities of pseudocapacitive metal sulfides, compositing them with organic carbon-based materials is proven to be an effective strategy.[14,15] Recently, NiCo$_2$S$_4$ and Ni$_3$S$_2$ have played a crucial role as promising electrode materials for pseudocapacitors due to their physical and chemical properties.[1,16] These materials exhibit better oxidation and reduction reactions due to the donation of Ni and Co ions, superior energy storing ability, but also exhibit drawbacks such as low energy density and structural damage over long cycles.[17–19] To address these issues, the composition of

[a] T. Arun, K. Aravinth, P. Balaji Bhargav
Department of Physics, SSN Research centre, Sri Sivasubramaniya Nadar College of Engineering, Kalavakam, Chennai, Tamilnadu 603110, India
E-mail: aravinthk@ssn.edu.in

[b] T. Arun, M. Govindasamy
International Ph.D. Program in Innovative Technology of Biomedical Engineering and Medical Devices, Ming Chi University of Technology, New Taipei City 243303, Taiwan
E-mail: manymany2025@mail.mcut.edu.tw

[c] M. Govindasamy
Research Center for Intelligence Medical Devices, Ming Chi University of Technology, New Taipei City 243303, Taiwan

Batteries & Supercaps

Research Article
doi.org/10.1002/batt.202400739

Chemistry Europe
European Chemical
Societies Publishing

materials and modification of structural morphologies, incorporating carbon to increase electrode conductivity and improve electrochemical behavior, have been explored. Several researchers are attempting to explore transition metal sulfide based materials for high performance supercapacitors.[20] Phonsuksawang et al. demonstrated Mn-doped Ni_3S_2/$NiCo_2S_4$ electrode achieving a specific capacitance of 1340 F/g, along with good cycling stability and rate capability.[21] Patil et al. reported $NiCo_2S_4$@Ni_3S_2 hybrid nano-needle array synthesized using metal-organic framework (MOF) precursor and subsequent sulfurization. This approach yielded an impressive specific capacitance of 1536.8 F/g at 1 A/g. Notably, their assembled asymmetric supercapacitor exhibited a superior energy density of 35.26 Wh/kg at a power density of 724.9 W/kg and maintained excellent capacitance retention (97.4%) after 10000 cycles.[22] Shobeiri et al. investigated core-shell structured $NiCo_2O_4$@Ni_3S_2 electrode, delivering a specific capacitance of 1800 F/g and retaining 98% capacitance after 2000 cycles.[23] Hu et al. further pushed the boundaries using $NiCo_2S_4$@CoAl LDH flower-shaped heterojunction nanosheets, achieving a remarkable specific capacitance of 2120 F/g @1 A/g. Additionally, their asymmetric supercapacitor displayed good energy and power density while maintaining 97.7% specific capacitance after 10000 cycles.[1]

The present work reports the development of a self-assembled and hierarchically structured CNF@NSNCS electrode material for supercapacitor applications. This novel electrode is a binder-free and eliminates the usage of additional polymers and simplifies the fabrication process. Our approach offers several advantages, including low cost, simple operation, and improved performance. Specifically, the binder-free design enhances both conductivity and specific surface area. This research investigates the feasibility of electrochemically promoting and controlling the in-situ growth of binder-free electrodes to achieve superior specific capacitance and high-current density behavior. The resulting asymmetric supercapacitor (ASC) exhibited a remarkable energy density of 77.5 Wh kg^{-1} at a power density of 748.4 W kg^{-1}, along with excellent cycle stability maintain 98.2% up to 13000 cycles. This work presents a straightforward and efficient method for improving the capacitance of metal sulfides and explores the potential of lignin as a valuable precursor for carbon materials in supercapacitors.

Experimental Section

Primary Materials

The materials used were of analytical grade and did not require any further processing before use. The starting materials included nickel (II) nitrate hexahydrate ($Ni(NO_3)_2 \cdot 6H_2O$), cobalt (II) nitrate hexahydrate ($Co(NO_3)_2 \cdot 6H_2O$), thiourea (NCH_4S), carbon nanofibers (CNFs), nickel foam (NF), acetone, ethanol, HCl, potassium hydroxide (KOH) pellets, and distilled water.

Synthesis of Ni_3S_2

A small piece of Ni foam (NF) substrate (3 cm×3 cm) was pre-treated ultrasonically with diluted HCl, acetone, and ethanol (10 minutes each) to remove surface contaminants. Subsequently, 0.025 M thiourea solution (180 mL) was prepared in distilled water under magnetic stirring. The pre-treated Ni foam and the clear thiourea solution were then transferred to a 200 mL stainless steel autoclave and heated at 180 °C for 12 hours. After the reaction, the resulting product was thoroughly washed and dried at 60 °C in hot air oven.

Synthesis of CNF@Ni_3S_2/$NiCo_2S_4$

A hierarchical nanostructure composed of carbon nanofibers (CNFs) embedded within a Ni_3S_2/$NiCo_2S_4$ composite (CNF@Ni_3S_2/$NiCo_2S_4$) was directly grown on nickel foam (3 cm×3 cm) using a facile in-situ hydrothermal method. First, Ni_3S_2 nanostructures were grown directly on the pre-cleaned Ni foam substrate following the procedure described in Section 2.2 (refer to Section 2.2 for details). Subsequently, 10 mg of CNFs, 0.5 mmol of nickel nitrate hexahydrate ($Ni(NO_3)_2 \cdot 6H_2O$), 1 mmol of cobalt nitrate hexahydrate ($Co(NO_3)_2 \cdot 6H_2O$), and 2 mmol of thiourea were dissolved in 180 mL of deionized (DI) water under magnetic stirring to form precursor solution. The pre-treated Ni foam with the pre-grown Ni_3S_2 and the prepared solution was then loaded into a 200 mL Teflon-lined stainless-steel autoclave and heated at 160 °C for 8 hours. After the reaction, the Ni foam electrode was thoroughly washed with DI water and ethanol, and dried at 60 °C overnight in convection oven. Similarly, Ni_3S_2/$NiCo_2S_4$ was prepared using same procedure for the comparison. The loading of mass of all electrodes was approximately ~3–4 mg/cm^2. The obtained electrode materials Ni_3S_2, Ni_3S_2/$NiCo_2S_4$ and CNF@Ni_3S_2/$NiCO_2S_4$ named as NS, NSNCS and CNF@NSNCS, respectively.

Material Characterization

In order to characterize the as-synthesized electrode, various analytical techniques were utilized. Here, we will explore each technique and the information it provides in detail. Powder X-ray diffraction (PXRD) was performed using a Bruker D2 Phaser with Cu−Kα radiation ($\lambda = 1.5406$ Å) in the 10°–60° 2θ range with a 0.02° step size at 45 kV and 40 mA. This technique helps to identify the crystal structure and phase of the material. X-ray photoelectron spectroscopy (XPS), employing a ULVAC-PHI PHI5000 Version probe III instrument, was used to examine the chemical composition and energy bands of the composite electrode. Field emission scanning electron microscopy (FESEM) was utilized to capture microstructure images and to reveal the surface morphology of the electrode. Energy-dispersive X-ray (EDX) microanalysis with mapping provided information on the chemical concentration and elemental composition of the synthesized material. Finally, high-resolution transmission electron microscopy (HRTEM) offered a high-resolution view of the internal morphology and elemental composition of the synthesized material.

Electrochemical Measurements

A standard three-electrode test system was employed to assess the electrochemical performance of the as-synthesized electrode materials using admiral electrochemical workstation (Squidstat, ±1 A). All the experiments were conducted in 6 M KOH aqueous solution under ambient conditions. The as-synthesized binder-free electrode materials were directly used as the working electrode. These electrodes had a dimension of 1 cm×1 cm and a mass

loading of active material ~3.5 mg/cm^2. Ag/AgCl electrode served as the reference electrode, while platinum wire functioned as the counter electrode.

The specific capacitances of as-synthesized electrodes are calculated from below equation.

$$C_{sp} = \frac{I \cdot \Delta t}{m \cdot \Delta V} F/g \tag{1}$$

Where I represents the current (mA), Δt signifies the discharge time (s), m denotes the active material mass (mg), and ΔV represents the operating potential window (V)

This approach aimed to evaluate the electrochemical performance of the fabricated devices, denoted as CNF@NSNCS//AC ASC devices. Here, as-synthesized electrode served as the positive electrode (cathode) and activated carbon functioned as the negative electrode (anode).

The specific capacitance within the asymmetric supercapacitor can be calculated using the following equation.

$$\frac{M^+}{M^-} = \frac{C^- \times \Delta V^-}{C^+ \times \Delta V^+} \tag{2}$$

In this equation, M^+ and M^- represent the mass loadings of active materials in the positive and negative electrodes, respectively. ΔV^+ and ΔV^- denote the operating potential windows of the positive and negative electrodes. C^+ and C^- represent the specific capacitances of the positive and negative electrodes.

Furthermore, the energy density and power density are calculated using the following equation.

$$E = \frac{0.5 * C_{sp}^* \Delta V2}{3.6} \ (Wh/kg) \tag{3}$$

$$P = \frac{3600^* E}{\Delta t} \ (W/Kg) \tag{4}$$

In these equations, Δt represents the discharge time, ΔV signifies the operating potential (V), and C_{sp} represents the specific capacitance (F/g).

2. Results and Discussion

The fabrication process of the hierarchical CNF@NSNCS network electrode is illustrated in Figure 1.

2.1. XRD Analysis

X-ray diffraction (XRD) spectroscopy, as shown in Figure 2, was employed to investigate the crystallographic information of the electrode. The peaks at 44.6° and 52.9° correspond to the (111) and (200) planes of Ni foam, respectively (denoted by '♦'). Additional peaks attributing to Ni_3S_2 (denoted by '♥') were observed at 21.8°, 31.2°, 37.8°, 49.7°, 50.2°, 55.1°, and 55.3°, matching to (101), (110), (003), (113), (211), (122) and (300) planes of rhombohedral Ni_3S_2, respectively (JCPDS card no. 44–1418). Similarly, distinct peaks (♣) corresponding to (311), (400), (511) and (440) planes of cubic $NiCo_2S_4$ (JCPDS card no. 43-1477) were identified at 31.5°, 38.1°, 50.6°, and 54.9°, indicating the presence of both Ni_3S_2 and $NiCo_2S_4$ in the samples.[21,24]
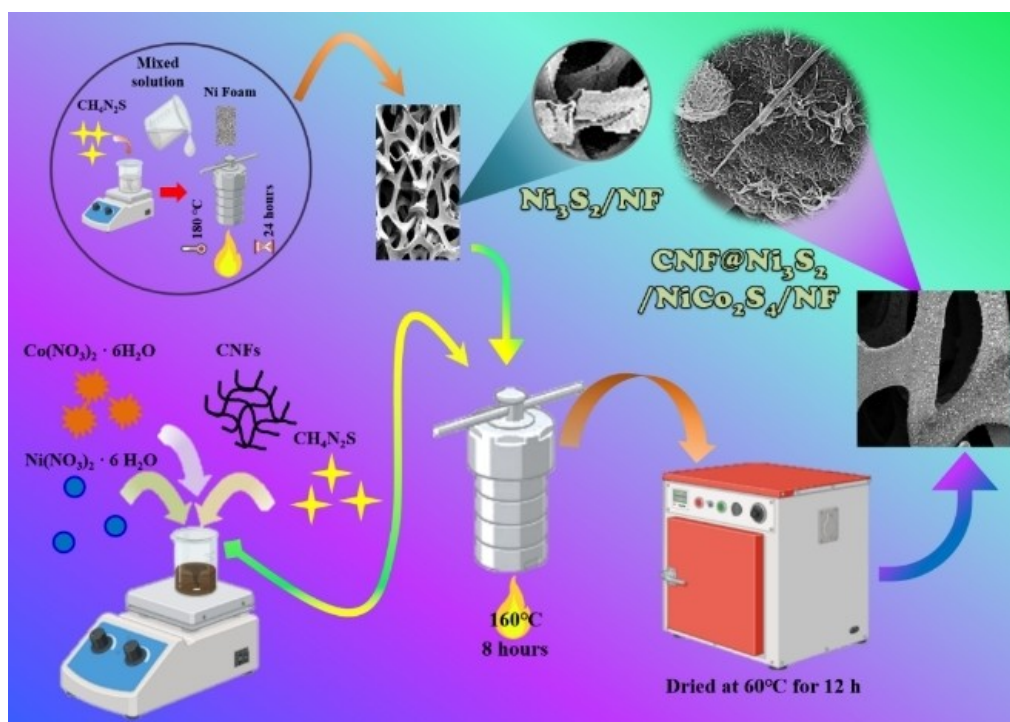

Figure 1. Schematic illustration of the synthesis process for CNF@NSNCS supercapacitor electrode.
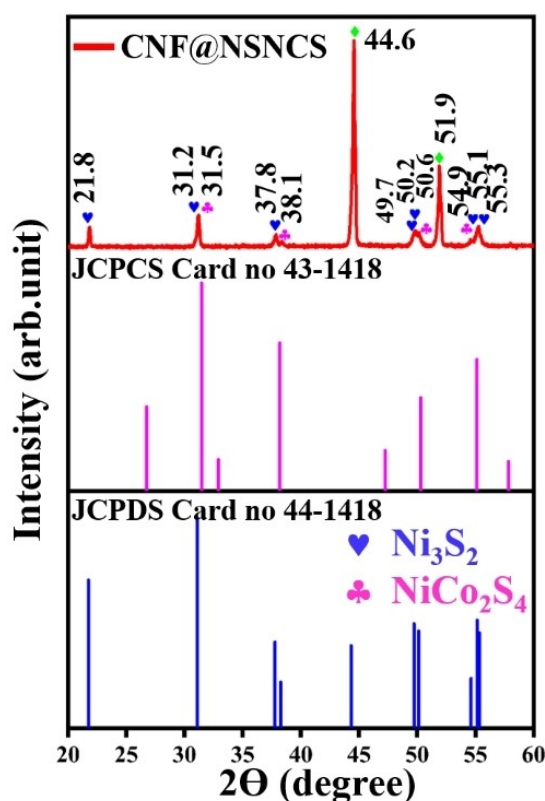
Figure 2. X-ray diffraction patterns of CNF@NSNCS.

Notably, the absence of characteristic carbon peaks suggests minimal CNF content, which is likely incorporated within the electrodes as evidenced by FESEM analysis.

2.2. Field Emission Scanning Electron Microscopy (FESEM) Analysis

Field Emission Scanning Electron Microscope (FESEM) analysis is employed to characterize the surface morphologies of the binder-free hybrid electrodes (Figure 3) at various magnifications. Figure 3(a–c) depicts pristine Ni_3S_2 microparticles with uniform coating on the Ni foam surface after the sulfurization process. These particles exhibit an irregular arrangement but are completely enveloped by a dense layer. The rough surface and numerous active sites of Ni_3S_2 are clearly visible. Figure 3(d) presents the composite electrode, where $Ni_3S_2/NiCo_2S_4$ exhibits layered growth on the Ni foam. The rough surface of Ni_3S_2 facilitates the in-situ growth of fully covered $NiCo_2S_4$ from the hydrothermal deposit. This layer exhibits vertical growth, with self-assembled hexagonal nanosheets forming an interconnected network on the Ni_3S_2 surface as shown in the magnified inset of Figures 3(e–f). Finally, the incorporation of CNF forms uniform and interconnected structure with high contact areas (Figure 3(g–i)). This is believed to promote rapid chemical growth and enhance the electrode's conductivity, leading to faster ion transport, improved electrolyte penetration, and ultimately resulting in enhanced electrochemical behavior. The

hierarchical structure exposes a high density of electrochemically active sites, facilitating easier ion/electron intercalation and de-intercalation within the layered structure.

Furthermore, Energy-dispersive X-ray spectroscopy (EDAX) mapping, as illustrated in Figure 4(a–f), is employed to investigate the elemental composition of the CNF@NSNCS hierarchical structure electrode. The EDAX analysis confirmed the uniform distribution of C, Ni, Co, and S elements throughout the composite, signifying the absence of impurities. This observation strongly supports the successful formation of the desired CNF@NSNCS hierarchical structure.

2.3. X-Ray Photoelectron Spectroscopy (XPS) Analysis

X-ray photoelectron spectroscopy (XPS) analysis is performed to investigate the chemical composition and oxidation states of the elements in the as-prepared CNF@NSNCS electrode structure. As illustrated in Figure 5(a), the Ni 2p spectrum exhibits two spin-orbit doublets at 855.6 eV and 873.4 eV, corresponding to Ni $2p_{3/2}$ and Ni $2p_{1/2}$, respectively. These peaks can be attributed to Ni^{2+} and Ni^{3+} ions. Additionally, two satellite peaks are observed at 861.0 eV and 879.6 eV.[20,25] Similarly, the Co 2p spectrum in Figure 5(b) displays spin-orbit doublets for Co $2p_{3/2}$ and Co $2p_{1/2}$ at 779.8 eV and 795 eV, respectively, suggesting the presence of both Co^{2+} and Co^{3+} ions.[21] Additionally, two satellite peaks are observed at 786.07 eV and 808.07 eV, respectively. The S 2p spectrum (Figure 5(c)) shows deconvoluted peaks at 162.2 eV and 163.2 eV, corresponding to S $2p_{3/2}$ and S $2p_{1/2}$, respectively. Finally, C 1s spectrum in Figure 5(d) presents three main peaks at 284.8 eV, 286.3 eV, and 288.7 eV. These peaks can be assigned to C—C bonds in the sp^2 graphite structure, C—O bonds associated with hydroxyl groups, and C=O bonds indicative of carboxy carbon, respectively.[26,27] The XPS analysis confirms the absence of impurities and the expected valence states of each element in the CNF@NSNCS hierarchical structure. These observations are consistent with the successful formation of the targeted hierarchical structure

2.4. High-Resolution Transmission Electron Microscopy (HRTEM) Analysis

High-resolution transmission electron microscopy (HRTEM) analysis is performed to investigate the microstructure and morphology of the as-synthesized binder-free CNF@NSNCS electrode (Figure 6). Figure 6(a–c) shows HRTEM images at various magnifications, clearly revealing the intimate integration of CNFs with the composite material. Ni_3S_2 and $NiCo_2S_4$ nanoparticles appear interconnected and the results are consistent with the observations from the FESEM analysis in Figure 3(g–i). Lattice fringes are evident in Figure 6(d–e), with d-spacing of 0.23 nm and 0.28 nm corresponding to the (400) and (311) planes of $NiCo_2S_4$, respectively.[28,29] Additionally, fringes with d-spacing of 0.21 nm, 0.16 nm, and 0.18 nm can be assigned to (101), (300), and (211) planes of Ni_3S_2, respectively. Finally, the selected area electron diffraction (SAED) pattern in
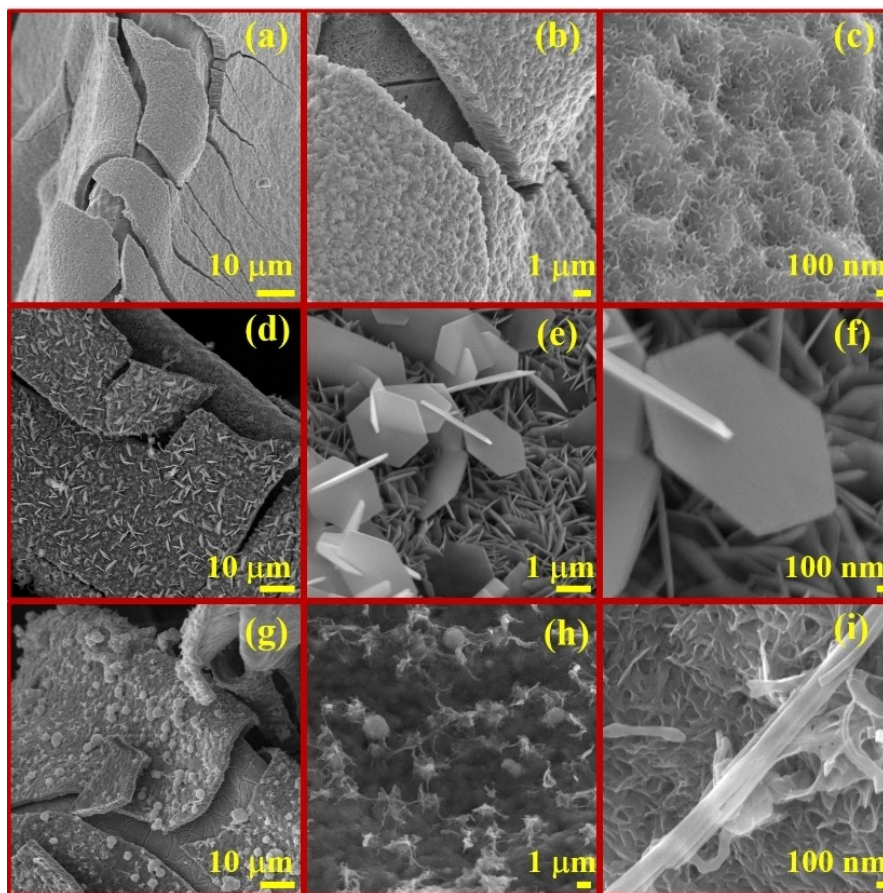
Figure 3. FESEM images (a) NS (10 μm), (b) NS (1 μm), (c) NS (100 nm), (d) NSNCS (10 μm), (e) NSNCS (1 μm) and (f) NSNCS (100 nm), (g) CNF@NSNCS (10 μm), (h) CNF@NSNCS (1 μm), (i) CNF@NSNCS (100 nm), at different magnifications.
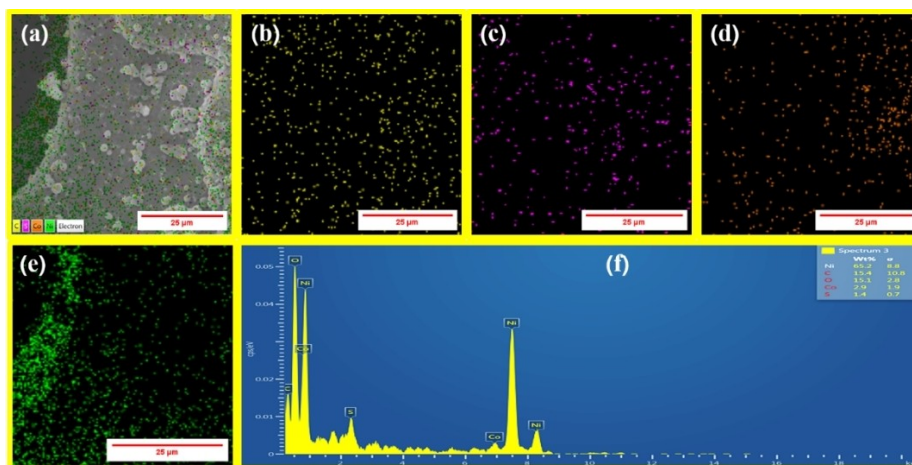

Figure 4. (a–f) The elemental composition of Energy Dispersive X- ray (EDX) microanalysis with mapping image of CNF@NSNCS electrode material.

Figure 6(f) confirms the highly crystalline nature of both Ni_3S_2 and $NiCo_2S_4$.[30] The observed d-spacing and crystal planes are consistent with and corroborated by the XRD analysis.

2.5. Three Electrode System

The electrochemical performance of the prepared electrodes was evaluated using cyclic voltammetry (CV), galvanostatic charge/discharge (GCD), electrochemical impedance spectroscopy (EIS) and cycle stability in a 6 M KOH electrolyte. Figure 7(a) compares the CV curves of NS, NSNCS, and
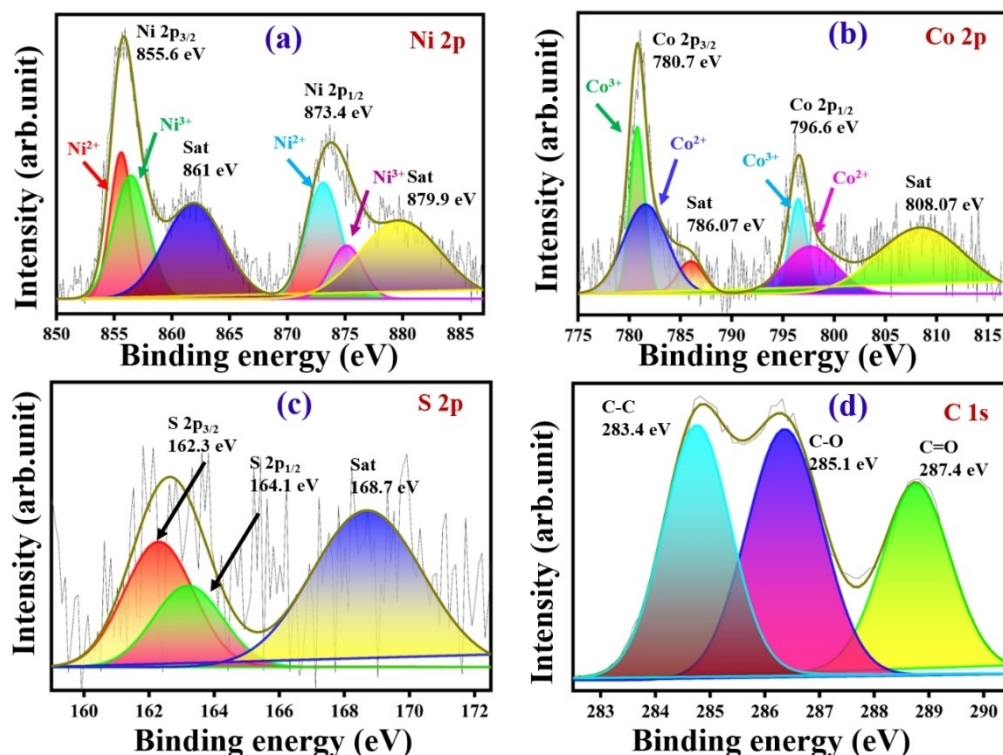
Figure 5. X-ray photoelectron spectroscopy (a) Ni 2p and (b) Co 2p (c) S 2p (d) C 1s of CNF@NSNCS nanocomposite material.
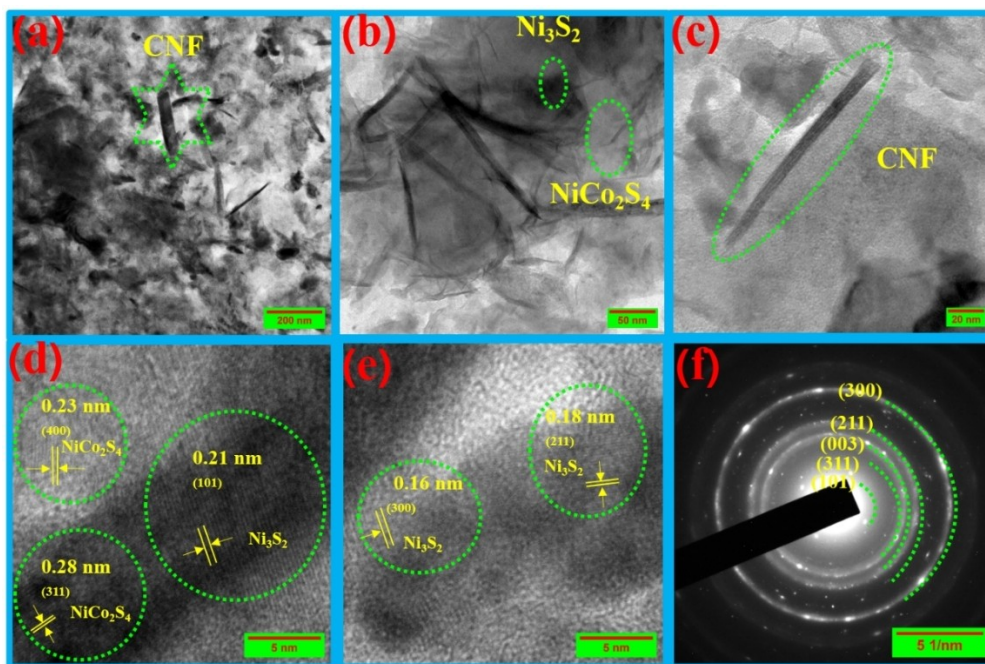

Figure 6. The high resolution transmission electron microscope image of CNF@NSNCS of electrode material (a) CNF@NSNCS (200 nm), (b) CNF@NSNCS (50 nm), (c) CNF@NSNCS (20 nm), (d–e) lattice fringe of Ni_3S_2 and $NiCo_2S_4$ (f) SAED pattern of CNF@NSNCS.

CNF@NSNCS electrodes at a scan rate of 5 mV/s within a potential window of 0–0.4 V (vs. Ag/AgCl). The hierarchical composite CNF@NSNCS electrode exhibits larger and more well-defined pair of redox peaks with greater enclosed area compared to the other electrodes. This indicates a larger specific capacitance and suggests that the incorporation of CNF provides superior capacity due to its high surface area. The CV curves of all synthesized electrodes reveal multiple anodic and cathodic peaks, signifying their battery-type characterstics and implying good charge transport and storage properties.[20]
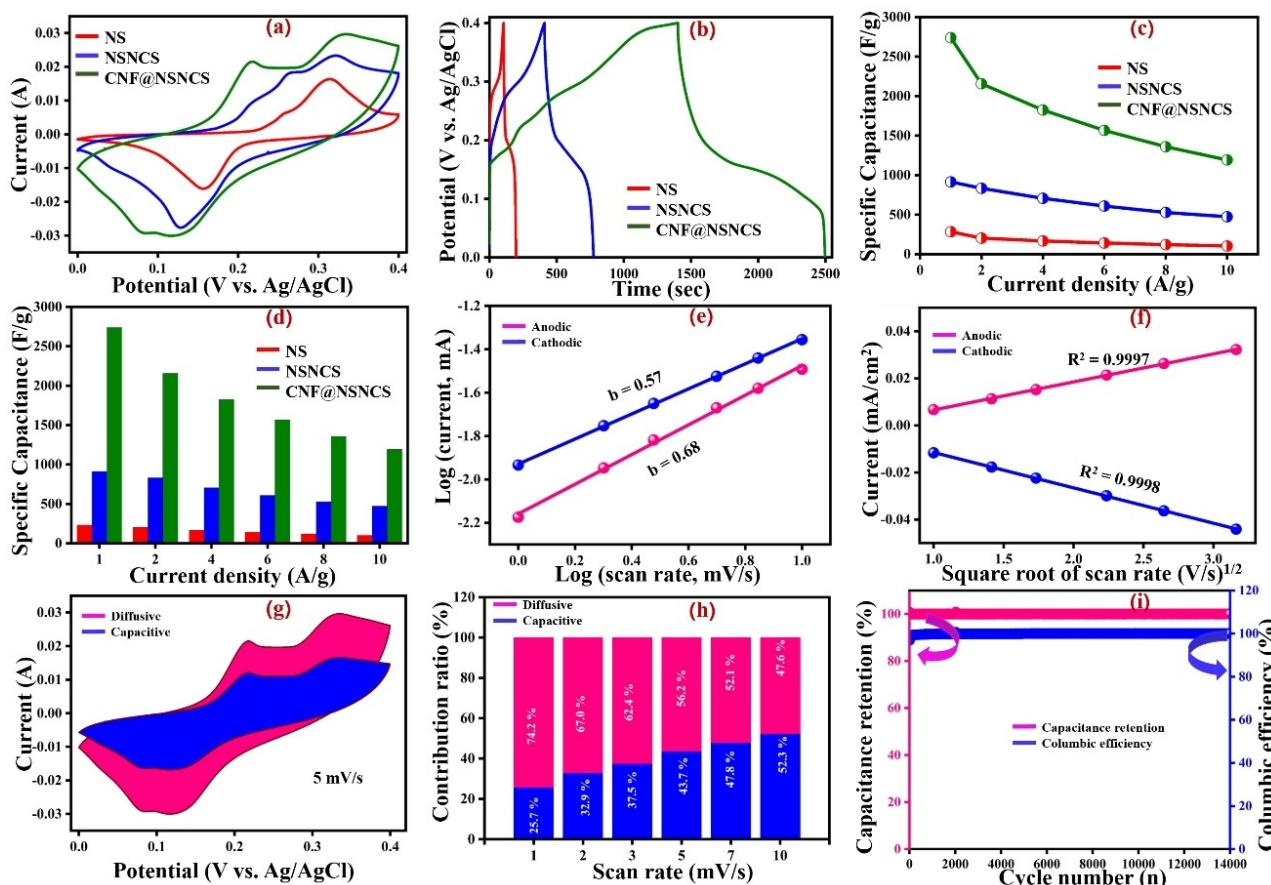
Figure 7. (a) CV curves of NS, NSNCS and CNF@NSNCS at 5 mV/s, (b) GCD curves of NS, NSNCS and CNF@NSNCS at 1 A/g, (c) Rate capability of NS, NSNCS and CNF@NSNCS, (d) Rate performance bar diagram of NS, NSNCS and CNF@NSNCS, (e) plot of log (current, mA) vs. log (scan rate, mV/s), (f) Dunn's plot, (g) Representative CV curve of capacitive and diffusive contributions of CNF@NSNCS at 5 mV/s, (h) De-convoluted capacitive and diffusive percentage contribution of CNF@Ni_3S_2/NSNCS at different low scan rates, (i) Cycle stability and columbic efficiency of CNF@NSNCS at a current density 20 A/g.

Interestingly, the incorporation of CNF appears to suppress the appearance of the smaller Co peaks in the CNF@NSNCS electrode under alkaline conditions.[21] Further CV investigations are conducted on individual electrode materials at various scan rates (10–100 mV/s) within the optimized potential window (0–0.4 V vs. Ag/AgCl). The results, presented in supporting information Figures S1 (a, b and c) demonstrate a typical behavior where the oxidation peaks shift positively and the reduction peaks shift negatively with increasing current due to faster ion intercalation and de-intercalation processes. The galvanostatic charge-discharge (GCD) profiles of all prepared electrodes within the optimized potential window (0–0.4 V vs. Ag/AgCl) are shown in Figure 7(b). The comparison of GCD curves reveals that the CNF@NSNCS electrode exhibits a significantly longer discharge time compared to the other electrodes. This enhanced performance is likely due to the combination of multiple metal oxidation states and the incorporation of conductive carbon, as evidenced by XPS and FESEM analyses. The specific capacitance values are calculated using Equation (1). At a current density of 1 A/g, the calculated specific capacitances for NS, NSNCS, and CNF@NSNCS electrodes are 233.82 F/g, 914 F/g, and 2738.5 F/g, respectively. These results demonstrate the significant improvement in capacitance

achieved with the CNF@NSNCS composite electrode. A comparison with other electrodes reported in previous studies, as detailed in Table 1, further underscores its superior performance.

Additional GCD investigations are performed on all synthesized electrodes at various current densities (1–10 A/g) within the potential window of 0–0.4 V (presented in supporting information Figures S1 (d, e and f)). As expected, the specific capacitance exhibits a decrease with increasing current density. This behavior can be attributed to the limitations imposed by the fast movement of charges and the ion intercalation/de-intercalation processes. Figure 7(c) illustrates the correlation between the specific capacitance of different samples and the current densities of NS, NSNCS, and CNF@NSNCS electrodes. The CNF@NSNCS hierarchical nanostructured electrode exhibited very high capacitance compared to other electrode materials due to the incorporation of CNF and self-assembled nanostructures with increased conductivity and electrochemical behaviour. When the current densities increased the specific capacitance of the electrode is decreased due to the drop in internal resistance (IR) at higher current densities. The calculated specific capacitances for all electrodes at different current

Batteries & Supercaps

Research Article
doi.org/10.1002/batt.202400739

Chemistry
Europe
European Chemical
Societies Publishing

Table 1. Specific capacitance of CNF@NSNCS-based hybrid electrodes compared with previously reported electrode materials in three-electrode systems.

S.No	Electrodes	Specific capacitance	Capacitance retention	Cycle stability	References
1	Mn doped $NiCo_2S_4/Ni_3S_2$	1350 (1 A/g)	160%	1000 Cycles	[21]
2	$NiCo_2O_4$@$NiCoMnS_4$	2508 (1 A/g)	87.80%	5000 Cycles	[31]
3	MnS@$NiCo_2S_4$	2372.7 (1 A/g)	78.2%	5000 cycles	[32]
4	$NiCo_2S_4$/rGO	1505 (1 A/g)	85.6%	5000 cycles	[33]
5	$NiCo_2S_4$/Carbon Aerogel	603 (1 A/g)	90%	5000 Cycles	[34]
6	Mo_2S_3@Ni_3S_2	998.9 (1 A/g)	90.55%	650 cycles	[35]
7	Nd doped Ni_3S_2	2122.64 (1 A/g)	–	–	[36]
8	$NiCo_2S_4$/BPC	175 (1 A/g)	–	–	[37]
9	**CNF@NSNCS**	**2738.5 (1 A/g)**	100%	**14000 Cycles**	**This Work**

densities are provided in Table 2, while the bar diagram in Figure 7(d) visually depicts this trend.

The charge storage mechanism in the CNF@NSNCS hierarchical structure electrode can be further evaluated using cyclic voltammetry (CV) curves at various slow scan rates (1–10 mV/s). Analysing these curves allows us to assess both the charge storage mechanism and the material type. The b-value is calculated using the following equation,

$$i = av^b$$

$$log(i) = bvlog(\nu)$$

Where, i is the current, v is the scan rate, and a & b are constants, provides valuable insights. b-value of 0.5 indicates a diffusion-controlled process, while a value of 1 suggests a surface-controlled mechanism. As shown in Figure 7(e), the b-values for the as-prepared CNF@NSNCS electrode are 0.68 and 0.57 for the anodic and cathodic processes, respectively. This suggests that the charge storage process is primarily governed by controlled surface diffusion. Additionally, Figure 7(f) demonstrates a linear increase in current with increasing scan rate, further supporting this conclusion. The following equations describe the differential contributions of surface diffusion and capacitive processes to the overall capacitance:

$$i = k_1v + k_2v^{1/2}$$

$$i/v^{1/2} = k_1v^{1/2} + k_2v$$

Where K_1V represents the surface-controlled capacitance and $K_2V^{1/2}$ reflects the diffusion-controlled contribution.

Furthermore, the CV curve of the CNF@NSNCS electrode at 5 mV/s (Figure 7(g)) suggests a combined mechanism involving both surface diffusion and capacitive processes. The calculated contribution ratios at different scan rates are presented in Supporting Information Figure S2(a–e). Notably, with increasing scan rate, the capacitive contribution increases, while the diffusion-controlled contribution decreases, likely due to faster ion intercalation and de-intercalation at the electrode surface (Figure 7(h)). Finally, the CNF@NSNCS involves as a long term cycle stability and columbic efficiency as shown in Figure 7(i). The experiment employed galvanostatic charge-discharge measurements at a current density of 20 A/g within the same optimized potential windows. The specific capacitance remained remarkably stable at 400 F/g even after 14,000 cycles, the specific capacitance retention 100% from its beginning level and the columbic efficiency 99.99%. This exceptional stability can be attributed to the electrode's self-assembled hierarchical structure and the absence of binders in its preparation. These features contribute to structural integrity and mitigate performance degradation during extended cycling. Ex-situ SEM and XRD analyses further confirm the electrode's stability. The SEM images reveal minor etching and deformation of the layered surface, along with slight detachment of incorporated CNFs, likely due to intercalation and de-intercalation reactions during cycling. Additionally, the presence of pores and voids in the binder-free electrode indicates extensive interaction with KOH electrolyte ions, as shown in the ex-situ SEM images (Figure S3(a–d)) (supporting information). XRD measurements performed on the cycled binder-free

Table 2. Specific capacitance values of NS, NSNCS and CNF@ NSNCS.

Electrodes	Current Density					
	@1 A/g (F/g)	@2 A/g (F/g)	@4 A/g (F/g)	@6 A/g (F/g)	@8 A/g (F/g)	@10 A/g (F/g)
NS	233.82	202.8	167.4	141	120.4	103
NSNCS	914.3	833.4	706.1	609.3	527.8	473.25
CNF@ NSNCS	2738.5	2155.9	1823.7	1566.6	1359.6	1192.2

Batteries & Supercaps

Research Article
doi.org/10.1002/batt.202400739

Chemistry Europe
European Chemical
Societies Publishing

CNF@NSNCS hierarchical structure electrode (Figure S4) (supporting information) provide further evidence of the electrode's structural integrity and cycling stability.

EIS analysis of the all electrodes is carried out at same condition with frequency range from 10^{-2} Hz–10^{5} Hz and the obtained results are as shown in Figure 8(a). The EIS curve revealed the conductive nature and ionic resistance of the electrode and electrolyte. It is observed that the Nyquist curve contains the arc at high frequency region and straight line occurs at the lower frequency region. The results showed that the internal resistance values (R_s) of NS, NSNCS and CNF@NSNCS are calculated to be 1.02 Ω, 0.94 Ω and 0.85 Ω, respectively. Here, CNF@NSNCS electrode showed the low resistance compared to other electrodes due to the composite formation of highly conducting materials, resulting in the decrease of internal resistance of CNF@NSNCS. In all electrode materials the charge transfer resistance is very much low.

In addition, EIS analysis is employed to investigate the charge transport and diffusion properties of the synthesized NS, NSNCS and CNF@NSNCS electrodes. The Warburg coefficient (σ_w) in the low frequency region of all electrode material. The calculated σ_w values for NS, NSNCS and CNF@NSNCS are 35.2 Ω cm²/s, 7.4 Ω cm²/s, and 0.41 Ω cm²/s, respectively. These results suggest a significant improvement in charge transport for CNF@NSNCS. This enhancement can be attributed to its unique features: high conductivity, self-assembled hierarchical structure, and the absence of binding polymers. These factors promote efficient electron transfer within the CNF@NSNCS electrode.

The primary mechanism for charge storage in these electrodes involves the diffusion of hydroxide (OH–) ions. The diffusion coefficient (D) of OH⁻ ions is calculated using the following equation.

$$D_{OH^-} = 0.5 \left(\frac{RT}{An^2F^2C\sigma_w} \right)$$

In this equation, R represented as gas constant, T is the temperature, A represents the area of the electrode, F represents the Faraday constant, C is represented by the concentration of OH⁻ ions in the electrolyte, and σ_w represented by the Warburg coefficient.[38]

The Warburg coefficient for each electrode is obtained from the low-frequency region of the EIS plot (Figure 8(b)) using the equation.

$$Z' = R_s + R_{ct} + \sigma_w\omega^{-0.5}$$

Here, Z' represents the real part of the impedance, and ω represents the angular frequency. The calculated D_{OH}^- values for NS, NSNCS and CNF@NSNCS are 5.446×10^{-5} cm^{-2} s^{-1}, 3.017×10^{-5} cm^{-2} s^{-1}, and 2.537×10^{-6} cm^{-2} s^{-1}, respectively. These results again highlight the superior performance of the CNF@NSNCS electrode, with a significantly higher diffusion coefficient value. This translates to faster and more efficient OH– ion diffusion within the electrode material.[39]

The real C'(ω) and imaginary C"(ω) parts of the capacitance are further analyzed using the following equations.

$$C'(\omega) = \frac{-Z''(w)}{w|Z(w)|^2 m}$$

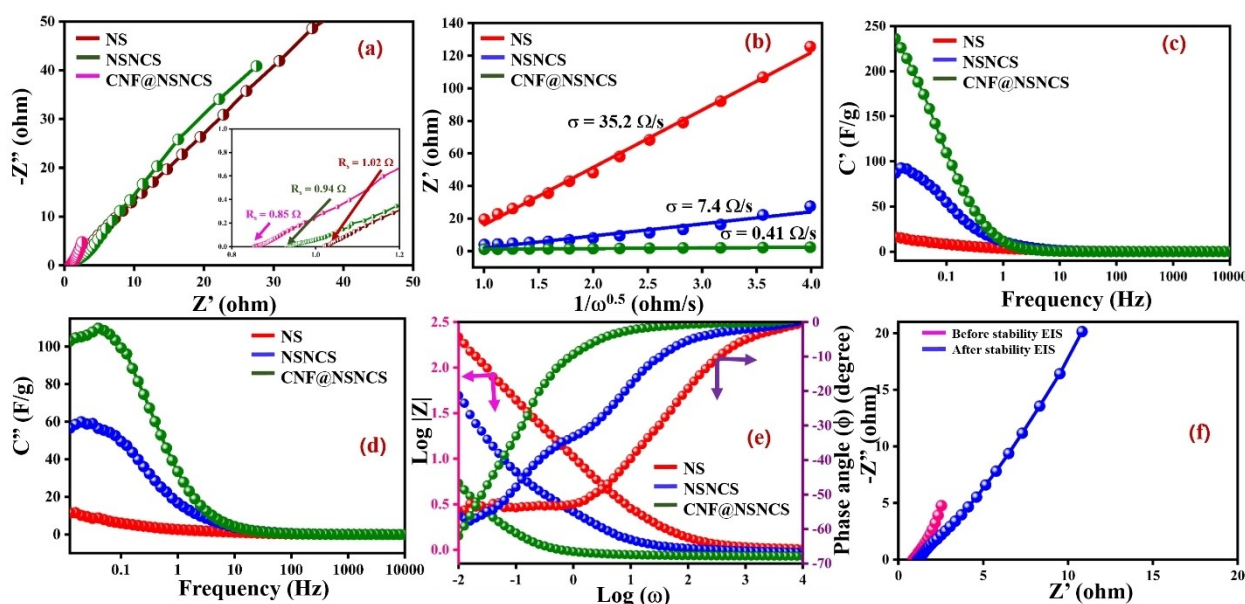$$C''(\omega) = \frac{-Z'(w)}{w|Z(w)|^2 m}$$

Figure 8. (a) EIS plot of NS, NSNCS and CNF@NSNCS, (b) Z' and $\omega^{-0.5}$ relationship plot at low frequency range of NS, NSNCS and CNF@NSNCS, (c) Real capacitance vs. frequency plot of NS, NSNCS and CNF@NSNCS, (d) Imaginary capacitance vs. frequency plot of NS, NSNCS and CNF@NSNCS, (e) Bode plot of NS, NSNCS and CNF@NSNCS (f) Before and after EIS plot of CNF@NSNCS.

Batteries & Supercaps

Research Article
doi.org/10.1002/batt.202400739

Chemistry
Europe
European Chemical
Societies Publishing

C'(ω) represents the real part of the capacitance, while C"(ω) relates to energy dissipation during charge storage processes. The CNF@NSNCS electrode exhibits a significantly higher real capacitance value C'(ω) (236 F/g) compared to NS (16 F/g) and NSNCS (86.8 F/g) (Figure 8(c)).[40] This indicates a greater ability to store charge in the CNF@NSNCS electrode. The imaginary part, C"(ω), is used to calculate the relaxation time constant (τ) using the equation,

$$\tau = \frac{1}{(2\prod f_0)}$$

Here, f_o represents the frequency at which the maximum imaginary capacitance is observed in the C"(ω) vs. frequency plot as shown in Figure 8(d). The relaxation times for NS, NSNCS and CNF@NSNCS are 17.9, 94.04, and 172.3 seconds, respectively.[38,40] Figure 8(e) presents the Bode plot of the electrochemical impedance, where the total impedance magnitude (log|Z|) and phase angle (φ) are plotted against the logarithmic frequency (log(ω)). This plot offers valuable insights into the resistive and capacitive behavior of the electrochemical system. In the Bode plot, a phase angle of 0° indicates a purely resistive element, while 90° signifies an ideal capacitor. Interestingly, all electrodes exhibit a phase angle of approximately 60° at very low frequencies, suggesting an enhanced capacitive response. Furthermore, the combined Bode plot demonstrates the frequency dependence of the impedance magnitude (|Z|) for all electrodes. As the frequency increases, the impedance magnitude decreases, indicating a transition from a more capacitive to a more resistive behavior.[41,42] Furthermore, Figure 8(f) compares the EIS curves of the CNF@NSNCS electrode before and after the long-term cycling test is conducted at the same frequency range. The internal resistance (R_s) increased slightly, from 0.85 Ω–1.13 Ω, while the charge transfer resistance (R_{ct}) increased due to the long time cycle stability. This could be due to the activation of the electrode during the cycling process. Furthermore, the experiment is conducted using a similar negative electrode for comparison. This electrode is subjected to identical experimental conditions as the activated carbon electrode under investigation. Performance evaluation is carried out using a three-electrode setup. Cyclic voltammetry (CV) scans are performed at various scan rates (5–100 mV/s) within an optimized potential window (−1−−0.8 V). Additionally, galvanostatic charge-discharge (GCD) curves are obtained at current densities ranging from 1–5 A/g. The calculated specific capacitance values for the activated carbon electrode at these current densities are found to be 417.5, 205.1, 129.18, 80, and 45.12 F/g, respectively. For a detailed visualization of these results, please refer to Figure S5(a–b) in the supplementary. The rate capability of the activated carbon electrode showed in Figure S5(c) (supporting information). At higher current densities, the specific capacitance of the electrode decreases, mainly due to internal resistance (IR) drops. Conversely, at a lower current density of 1 A/g, slower ion diffusion results in longer charge/discharge times, as the adsorption and desorption processes occur more gradually.

2.6. Two Electrode System

The electrochemical performance of the CNF@NSNCS//AC asymmetric supercapacitor electrodes is evaluated using cyclic voltammetry (CV), galvanostatic charge-discharge (GCD), and electrochemical impedance spectroscopy (EIS). Figure 9(a) shows the CV curves of the individual half-cells (CNF@NSNCS positive electrode and AC negative electrode), demonstrating their respective electrochemical behaviour. The mass loading of both electrodes is balanced using a mass balance equation (Equation (2)) to achieve optimal performance. The assembled device is optimized by CV with different potential ranges of 0-1.2-0-1.6 V, as shown in Figure 9(b). The results suggest that the device can successfully operate at 1.5 V with good reversibility, but increasing the potential further may initiate water splitting. The assembled device exhibited non-symmetrical CV curves at various scan rates (5–100 mV/s) within an optimized potential window of 0–1.5 V, as seen in Figure 9(c), indicating a hybrid charge storage mechanism. Interestingly, the distorted shape of the CV curves suggests a hybrid capacitance behaviour of the device. The lack of change in the CV curves with increasing scan rate indicates good rate capability. Similarly, GCD curves are measured at different current densities (1–10 A/g) within the same potential window, as shown in Figure 9(d). The non-similar, slight voltage drop, in the charge-discharge profiles reflects the combined redox-mediated and pseudocapacitive (hybrid) charge storage processes. The specific capacitance of the device, calculated using Equation (1), is found to be 248, 211.5, 104.4, 51.8, and 10 F/g at current densities of 1, 1.5, 2, 2.5, and 3 A/g, respectively. Additionally, the rate capability of the CNF@NSNCS//AC device decreased with increasing current density, as shown in Figure 9(e). The energy and power densities are further calculated using Equations (3) and (4), revealing a trade-off between these parameters as shown in the Ragone plot, Figure 9(f). The assembled device exhibited a maximum energy density that decreased from 77.5–3.12 Wh/kg as the power density increased from 748.4–2250 W/kg, respectively. The obtained results are also compared to previous research results and are shown in Table 3.

The long-term cycling stability and columbic efficiency, crucial for supercapacitor applications, are assessed (Figure 9(g)). The device displayed remarkable stability, retaining 98.2% capacitance and achieving 99.5% columbic efficiency after 13,000 cycles at a current density of 2.5 A/g. This indicates excellent cycling performance. From Figure 9(h), EIS analysis provided insights into the electron/ion transport and conductivity of the electrodes. The observed internal resistance (R_s) and charge transfer resistance (R_{ct}) of the CNF@NSNCS//AC electrode before and after long term cycle stability 19.3 Ω and 20.07 Ω&6.93 Ω and 9.11 Ω, respectively, signifying good conductivity due to the minimal charge transfer resistance. However, these values slightly increased during long-term cycling, likely due to the dynamic ion adsorption/desorption process and gradual electrolyte degradation. Finally, Figure 9(i) presents the Bode plot of the electrochemical impedance, where the total impedance magnitude (log|Z|) and phase angle (f) are plotted against the logarithmic frequency (log(w)),

Batteries & Supercaps

Research Article
doi.org/10.1002/batt.202400739

Chemistry Europe
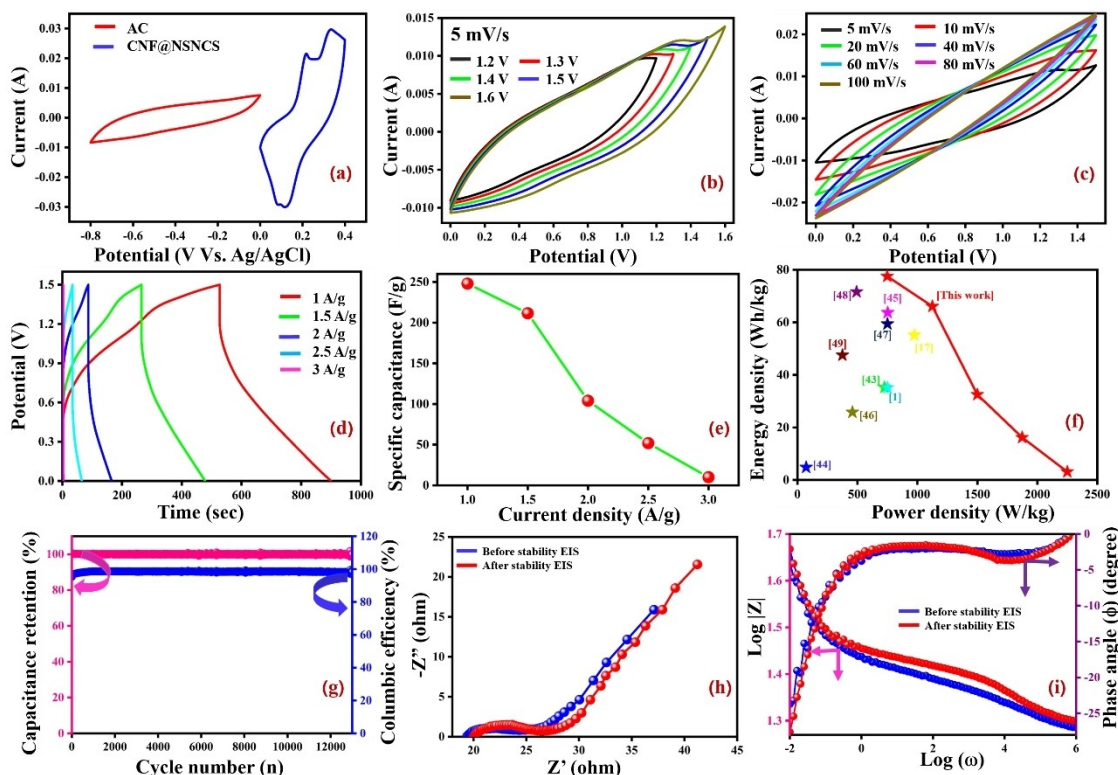European Chemical
Societies Publishing

Figure 9. (a) CV curves of CNF@NSNCS and AC at 5 mV/s, (b) Different potential windows of CV curves of CNF@NSNCS//AC device at 5 mV/s, (c) CV curves of CNF@NSNCS//AC different scan rates, (d) GCD curves of CNF@NSNCS//AC different current densities, (e) Rate capability of CNF@NSNCS//AC ASC device, (f) Ragone's plot of Dunn's plot CNF@NSNCS//AC ASC device, (g) Cycle stability and columbic efficiency of CNF@NSNCS//AC ASC device at a current density 2.5 A/g (h) Before and after EIS plot of CNF@NSNCS//AC ASC device, (i) Before and after cyclic stability Bode plot of CNF@NSNCS//AC ASC device.

Table 3. A comparison of the energy density and power density of the assembled device.

S. No	Device	Energy density (Wh/kg)	Power density (W/kg)	Reference
1	$NiCo_2S_4@Ni_3S_2//AC$	35.26	724.93	[43]
2	Ni_3S_2-MoS_2-$CeO_2//AC$	4.84	72	[44]
3	$NiCo_2S_4@CoAl$-LDH//AC	35.1	751.2	[1]
4	Ni_3S_2/rGO-90//AC	63.7	752.3	[45]
5	Ni@rGO–Co_3S_4//Ni@rGO-Ni_3S_2	55.16	975	[17]
6	Ni_3S_2/CNTs//CNTS	25.8	458	[46]
7	$NiCo_2S_4@N$-CNTs//AC	59.37	750	[47]
8	$NiCo_2S_4$/Polyaniline/MnO_2//N, S–Co-Doped Carbon	71.6	492.7	[48]
9	$NiCo_2S_4$/MC//MC	47.5	375	[49]
10	**CNF@NSNCS//AC**	**77.5**	**748.4**	**This Work**

indicating the resistive and capacitive behaviour of the device. In the Bode plot, a phase angle of ~30° at very low frequency, which suggest that the capacitive behaviour and the combined Bode plot demonstrates the frequency dependence of the impedance magnitude (|Z|) for assembled cell. As the frequency increases, the impedance magnitude decreases, indicating a transition from a more capacitive to a more resistive behavior.

To demonstrate the practical application of the fabricated CNF@NSNCS//AC ASC device, we successfully powered a commercial red LED. Three coin cell batteries are connected in series and used as the power source. As illustrated in Figure 10(a), the LED is then connected to the series-connected devices. Upon a single charge, the commercial LED illuminated for a duration of 35 minutes. The corresponding photographs are presented in Figure 10(b–e).
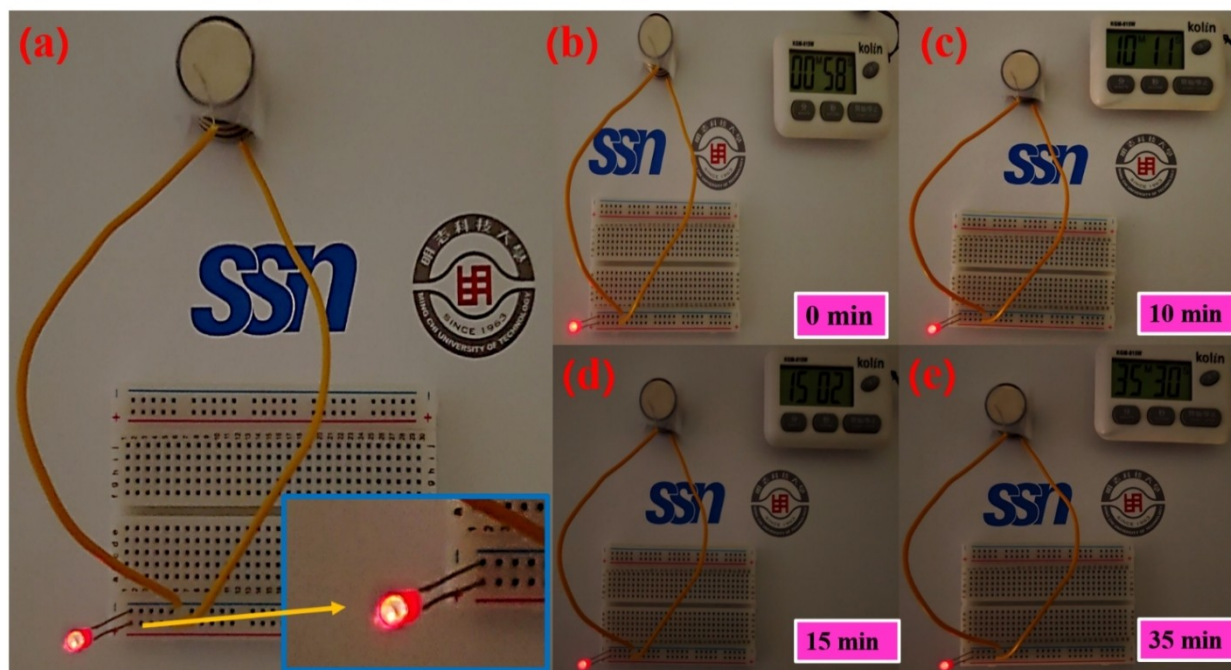
Figure 10. (a) Digital photographic images of commercial red LED light glowing, (b–e) Different timeline photographic images of glowing red LED being powered by CNF@NSNCS//AC ASC device.

3. Conclusions

In this work, we successfully designed a simple chemical growth of hierarchical structure electrode without any external use of binding polymers by hydrothermal method. The self-assembled structures of uniformly coated active materials enhanced the electrochemical performance and conductivity. The resulting CNF@NSNCS hierarchical structure electrode exhibited a superior electrochemical performance with high specific capacitance of 2738.5 at 1 A/g with superior rate capability performance and cyclic performance. In addition, the assembled CNF@NSNCS//AC two electrode cell achieved very high specific capacitance of 248 F/g at 1 A/g and good cycle stability. Furthermore, the CNF@NSNCS//AC assembled cell achieved superior energy density 77.5 Wh/kg with corresponding power density 748.4 W/kg and excellent cycle stability with 98.2% capacitance retention after 13000 cycles and the assembled CNF@NSNCS//AC devices were used in the field supercapacitor application such as red LED light glowing. These results opens a new avenue for rational designing and a great role of future energy storage application.

Conflict of Interests

The authors declare no conflict of interest.

Data Availability Statement

The data that support the findings of this study are available from the corresponding author upon reasonable request.

[1] J. Hu, Y. Pan, Q. Zhang, Z. Dong, S. Han, *Energy Fuels* **2024**, *38*(7), 6459–6470.
[2] T. Arun, K. Aravinth, P. B. Bhargav, M. K. Francis, *J. Phys. Chem. Solids* **2024**, *184*, 111723.
[3] K. N. Sathya Sai, A. S. Darsan, K. Wang, A. Pandikumar, S. M. Venkatakrishnan, Z. Hong, *ACS Appl. Nano Mater.* **2024**, *7*(10), 11931–11941.
[4] J.-A. Chou, S.-H. Kao, T.-Y. Chen, M. Mathankumar, S.-Y. Wei, C.-H. Su, J.-Y. Lin, C.-K. Hsieh, *J. Alloys Compd.* **2024**, *1002*, 175257.
[5] C.-S. Dai, P.-Y. Chien, J.-Y. Lin, S.-W. Chou, W.-K. Wu, P.-H. Li, K.-Y. Wu, T.-W. Lin, *ACS Appl. Mater. Interfaces* **2013**, *5*(22), 12168–12174.
[6] J. Ramadoss, A. Sonachalam, M. Govindasamy, *Energy Fuels* **2023**, *37*(22), 17561–17574.
[7] N. Zong, J. Wang, Z. Liu, S. Wu, X. Tong, Q. Kong, R. Xu, L. Yang, *Energies* **2024**, *17*(11), 2788.
[8] J. Sun, X. Tian, C. Xu, H. Chen, *J. Mater.* **2021**, *7*(6), 1358–1368.
[9] H. Sun, Y. Miao, G. Wang, X. Han, C. Xu, J. Zhu, H. Chen, *J. Energy Storage* **2024**, *92*, 112189.
[10] Y. He, L. Li, X. He, C. Liu, T. M. Aminabhavi, Y. Vasseghian, A. Hojjati-Najafabadi, *ACS Appl. Nano Mater.* **2024**, *7*(11), 12701–12710.
[11] J. Yu, Z. Hou, H. Zhang, X. Zhou, *Fuel* **2024**, *357*, 129754.
[12] S. Liu, J. Wu, X. Wang, S. He, J. Yang, *Chem. Eng. Sci.* **2024**, *293*, 120065.

Batteries & Supercaps

Research Article
doi.org/10.1002/batt.202400739

Chemistry
Europe

European Chemical
Societies Publishing

[13] T. Ahmad, B. M. Alotaibi, A. W. Alrowaily, H. A. Alyousef, M. F. Alotiby, M. Abdullah, A. Dahshan, A. M. A. Henaish, S. Aman, *Ceram. Int.* **2024**, *50*(9), 15100–15109.

[14] H. Wang, W. Zhang, X. Zhang, S. Hu, Z. Zhang, W. Zhou, H. Liu, *Nano Res.* **2021**, *14*(12), 4857–4864.

[15] W. Chen, P. Yuan, S. Guo, S. Gao, J. Wang, M. Li, F. Liu, J. Wang, J. P. Cheng, *J. Electroanal. Chem.* **2019**, *836*, 134–142.

[16] H. Chen, E. Bao, H. Sun, H. Ren, X. Han, Y. Wang, Z. Zhang, C. Luo, C. Xu, *J. Colloid Interface Sci.* **2024**, *664*, 117–127.

[17] D. Ghosh, C. K. Das, *ACS Appl. Mater. Interfaces* **2015**, *7*(2), 1122–1131.

[18] X. Han, H. Sun, C. Xu, J. Zhu, H. Chen, *J. Colloid Interface Sci.* **2024**, *667*, 350–361.

[19] X. Ren, L. Ren, Y. Hu, H. Sun, X. Han, C. Xu, H. Chen, *Colloids Surf. A Physicochem. Eng. Asp.* **2024**, *703*, 135395.

[20] X. Xu, Q. Liu, W. Zhong, L. Zhang, Y. Lu, Y. Du, *Int. J. Hydrogen Energy* **2021**, *46*(79), 39226–39235.

[21] P. Phonsuksawang, P. Khajondetchairit, K. Ngamchuea, T. Butburee, S. Sattayaporn, N. Chanlek, S. Suthirakun, T. Siritanon, *Electrochim. Acta* **2021**, *368*, 137634.

[22] S. J. Patil, J. H. Kim, D. W. Lee, *Chem. Eng. J.* **2017**, *322*, 498–509.

[23] M. Shobeiri, K. Tahmasebi, S. M. A. Hosseini, *J. Electron. Mater.* **2023**, *52*(10), 6416–6424.

[24] H. Liu, X. Ma, Y. Rao, Y. Liu, J. Liu, L. Wang, M. Wu, *ACS Appl. Mater. Interfaces* **2018**, *10*(13), 10890–10897.

[25] J. Lin, Y. Yan, X. Zheng, Z. Zhong, Y. Wang, J. Qi, J. Cao, W. Fei, Y. Huang, J. Feng, *J. Colloid Interface Sci.* **2019**, *536*, 456–462.

[26] H. Lin, F. Liu, X. Wang, Y. Ai, Z. Yao, L. Chu, S. Han, X. Zhuang, *Electrochim. Acta* **2016**, *191*, 705–715.

[27] F. Xie, H. Zhu, Y. Qu, J. Hu, H. Tan, K. Wang, L. Sun, *J. Colloid Interface Sci.* **2024**, *657*, 63–74.

[28] Y. Zhang, X. Wang, M. Shen, X. Fu, M. Huang, X. Liu, Y. X. Zhang, *J. Mater. Sci.* **2019**, *54*(6), 4821–4830.

[29] Y. Chen, L. Wang, H. Gan, Y. Jiang, J. Feng, J. Liu, X. Shi, *J. Energy Storage* **2022**, *47*, 103625.

[30] J. Wang, Y. Xie, L. Wang, L. Wang, L. Yue, D. Jin, *Mater. Res. Bull.* **2020**, *131*, 110957.

[31] Z. Yu, E. Liu, K. Xu, X. Yao, M. Wei, C. Jiehu, **2024**, Hierarchical Nanoflower-Like Nico2o4@Nicomns4 Composite with High-Performance Asymmetric Supercapacitor, DOI: 10.2139/ssrn.5059714

[32] X. Wang, S. Ren, D. Kong, C. Liu, Y. Wu, *J. Phys. Conf. Ser.* **2024**, *2842*(1), 012092.

[33] A. J. Ahamed, P. Kanagambal, *Chem. Phys. Impact* **2024**, *9*, 100675.

[34] P. Hao, J. Tian, Y. Sang, C.-C. Tuan, G. Cui, X. Shi, C. P. Wong, B. Tang, H. Liu, *Nanoscale* **2016**, *8*(36), 16292–16301.

[35] S. F. Niu, J. H. Zheng, *J. Alloys Compd.* **2018**, *737*, 809–814.

[36] A. BaQais, M. A. Amin, S. Aman, S. R. Ejaz, H. M. T. Farid, Z. M. El-Bahy, *Electrochim. Acta* **2023**, *467*, 143070.

[37] J. Feng, X. Zhang, Q. Lu, E. Guo, M. Wei, *Energy Fuels* **2022**, *36*(10), 5424–5432.

[38] K. K. Raja, V. Kumar, *J. Phys. Chem. C* **2024**, *128*(16), 6600–6611.

[39] C. An, Y. Yuan, B. Zhang, L. Tang, B. Xiao, Z. He, J. Zheng, J. Lu, *Adv. Energy Mater.* **2019**, *9*(18), 1802695.

[40] E. Y. L. Teo, H. N. Lim, R. Jose, K. F. Chong, *RSC Adv.* **2015**, *5*(48), 38111–38116.

[41] V. Sankar Devi, K. Kannadasan, P. C. Sharafudeen, P. Elumalai, *New J. Chem.* **2022**, *46*(31), 15130–15144.

[42] S. A. Kumar, A. Gowdhaman, C. Balaji, R. Ramesh, P. M. Anbarasan, *Colloids Surf. A Physicochem. Eng. Asp.* **2024**, *685*, 133247.

[43] C. Chen, J.-J. Zhou, Y.-L. Li, Q. Li, H.-M. Chen, K. Tao, L. Han, *New J. Chem.* **2019**, *43*(19), 7344–7349.

[44] M. Bhosale, N. Baby, S. S. Magdum, N. Murugan, Y. A. Kim, S. Thangarasu, T.-H. Oh, *J. Energy Storage* **2024**, *80*, 110301.

[45] F. Fei, H. Zhou, Y. Liu, F. Li, Q. Wang, P. Wen, *Mater. Today Commun.* **2024**, *38*, 108346.

[46] W. Yu, W. Lin, X. Shao, Z. Hu, R. Li, D. Yuan, *J. Power Sources* **2014**, *272*, 137–143.

[47] Y. Ye, Y. Luo, J. Lou, X. Chen, Y.-J. Cheng, J. Xia, Y. Li, K. Guo, *ACS Appl. Energy Mater.* **2023**, *6*(12), 6742–6751.

[48] Z. Karami, F. Hekmat, M. Chougale, S. Shahrokhian, D. P. Dubal, *Small* **2024**, *20*(45), 2404506.

[49] L. Qin, Z. Cui, Z. Hou, Y. Li, *J. Energy Storage* **2024**, *97*, 112873.